# Solving the nanostructure problem: exemplified on metallic alloy nanoparticles†

Valeri Petkov,*[a] Binay Prasai,[a] Yang Ren,[b] Shiyao Shan,[c] Jin Luo,[c] Pharrah Joseph[c] and Chuan-Jian Zhong[c]

With current technology moving rapidly toward smaller scales nanometer-size materials, hereafter called nanometer-size particles (NPs), are being produced in increasing numbers and explored for various useful applications ranging from photonics and catalysis to detoxification of wastewater and cancer therapy. Nature also is a prolific producer of useful NPs. Evidence can be found in ores on the ocean floor, minerals and soils on land and in the human body that, when water is excluded, is mostly made of proteins that are 6–10 nm in size and globular in shape. Precise knowledge of the 3D atomic-scale structure, that is how atoms are arranged in space, is a crucial prerequisite for understanding and so gaining more control over the properties of any material, including NPs. In the case of bulk materials such knowledge is fairly easy to obtain by Bragg diffraction experiments. Determining the 3D atomic-scale structure of NPs is, however, still problematic spelling trouble for science and technology at the nanoscale. Here we explore this so-called "nanostructure problem" from a practical point of view arguing that it can be solved when its technical, that is the inapplicability of Bragg diffraction to NPs, and fundamental, that is the incompatibility of traditional crystallography with NPs, aspects are both addressed properly. As evidence we present a successful and broadly applicable, 6-step approach to determining the 3D atomic-scale structure of NPs based on a suitable combination of a few experimental and computational techniques. This approach is exemplified on 5 nm sized $Pd_xNi_{100-x}$ particles ($x = 26$, 56 and 88) explored for catalytic applications. Furthermore, we show how once an NP atomic structure is determined precisely, a strategy for improving NP structure-dependent properties of particular interest to science and technology can be designed rationally and not subjectively as frequently done now.

## Introduction

The three-dimensional (3D) atomic structure of bulk single crystals can be determined with high precision, *i.e.* "solved" as the scientific community tends to emphasize, by analysing the positions and intensities of thousands of sharp Bragg peaks usually present in their 3D diffraction patterns.[12,13] The situation with bulk polycrystalline materials, which are ensembles of micrometer-size crystallites and so often referred to as "powders", is somewhat complicated due to the one dimensional (1D) character of their diffraction patterns reducing the

number of sharp Bragg peaks to a few hundreds at best. Nevertheless, solving a crystal structure on the basis of powder diffraction data has been increasingly successful,[14] thanks to the recent advances in X-ray instrumentation allowing collection of powder diffraction patterns with excellent resolution[15] and computer power allowing implementation of sophisticated algorithms[16,17] for reconstructing 3D atomic ordering from the less informative, when compared to the case of single crystals, 1D diffraction data at hand. Typically, a solved crystal structure is represented in terms of positions of atoms in a unit cell of a perfectly periodic, infinite 3D lattice. This is possible because atoms in bulk crystalline materials are arranged in full accord with such, also known as Bravais, lattices. The Bravais lattice type, lattice cell size and positions of atoms in the cell are so selected that the solved crystal structure is represented both very accurately and as concisely as possible. From the positions of atoms in the cell all essential structural characteristics of the bulk crystalline material studied such as, for example, atomic bond lengths and angles, atomic coordination types and numbers, chemical species arrangement patterns, hereafter called chemical patterns, local symmetry, *etc.* can be obtained

*[a] Department of Physics, Central Michigan University, Mt. Pleasant, Michigan 48859, USA. E-mail: petko1vg@cmich.edu; Fax: +1-989-774-2697; Tel: +1 989 774 3395*

*[b] X-ray Science Division, Advanced Photon Source, Argonne National Laboratory, Argonne, Illinois 60439, USA. E-mail: yren@anl.gov; Fax: +1-630-252-0365; Tel: +1-630-252-8651*

*[c] Department of Chemistry, State University of New York at Binghamton, New York 13902, USA. E-mail: cjzhong@binghamton.edu; Fax: +1-607-777-4478; Tel: +1-607-777-4605*

and, hence, the relationship between the crystal's atomic structure and properties explored straightaway.

Precise determination of the 3D atomic structure of NPs, which are ensembles of particles smaller than several tens of nanometers in at least one dimension,[1-10] is, however, far more complicated and so has become known as the "nanostructure problem".[11] The problem has both technical and fundamental aspects. In particular, similar to polycrystalline ensembles, NP ensembles exhibit 1D diffraction patterns. However, contrary to the case of polycrystalline ensembles, the 1D diffraction patterns for NP ensembles do not show a series of sharp Bragg peaks but only a few broad, Bragg-like features merged into an irregular, low-frequency oscillation (*e.g.* see Fig. S1† introduced later on). This renders the well-established, sharp Bragg peak-based procedures for determining the 3D atomic structure *technically impossible* to apply to NPs. Furthermore, the surface to volume ratio in NPs is much larger than that in bulk crystalline materials rendering the percentage of surface atoms in the former much larger than that in the latter. For example, about 45% and 10% of all atoms in particles with a spherical shape and size of 5 nm and 50 nm, respectively, are surface atoms. Atoms at NP surfaces have incomplete coordination spheres,[18] experience significant surface relaxation[19] and, quite often, surface environment[20] effects. As a result, atoms at NP surfaces and atoms inside NPs, that have complete coordination polyhedra and are largely not affected by NP extended surface related effects, may not exhibit the same structural pattern. Therefore, intrinsically, atoms in significant fractions of NPs, in particular NP surface and NP core atoms, may not arrange alike.[18-21] Besides, in pursuit of particular functionality, the arrangement of atoms in NPs is often made extra irregular deliberately.[22,23] Thus, more often than not, the underlying concept of traditional crystallography that like atoms occupy like positions in perfectly periodic, infinite 3D lattices appears *fundamentally broken* with finite size, extended free surface NPs. Therefore, positions of atoms in unit cells of perfectly periodic, infinite 3D lattices may not represent the atomic structure of NPs accurately but approximate it to a certain extent only,[23] if at all.[24] Evidently, given the fundamental incompatibility of traditional crystallography with NPs, the positions of all and not a small, pre-selected fraction of atoms in a nanometer-size material under study should be determined and used when the relationship between the NP atomic structure and properties is to be explored accurately. This, as shown here, can be a fairly achievable task.

Over the years the technical and fundamental aspects of the "nanostructure problem"[11] have been addressed in a number of studies. For example, some studies have concentrated[25] on resolving the problem's technical aspect and so considered the rather diffuse diffraction patterns of NPs not in reciprocal but in real space in terms of atomic Pair Distribution Functions (PDFs), introduced later on. However, unit cells of perfectly periodic, infinite 3D lattices have been made use of and, hence, the atomic structure of NPs studied has not been solved but only approximated. Other studies[26] have taken a step further by considering NPs' finite size and extended surface. These studies, however, have featured NPs as nanometer-size replicas

of perfectly periodic crystals and so have not quite crossed the limits of traditional crystallography. Studies based on experimental atomic PDFs and finite size atomic structure models built by molecular dynamics simulations[27] or constructed semi-manually as to resemble crystal structure types of interest[28] have proven more successful. The models, however, have been approached from more of a qualitative than of a quantitative point of view and so the atomic structure of NPs studied has not been determined precisely. Concentrating on resolving the problem's fundamental aspect, some studies have pursued constructing NP structure models from scratch, *i.e.* starting with a small pile of uncorrelated and not prearranged, in a particular way, atoms. These, *ab initio* type studies proved successful only in the case of 0.7 nm in size $C_{60}$ molecules (buckminsterfullerene) with well-known in advance, soccer ball-type structure.[29,30] By contrast, other studies have employed a bulk crystal-based approach to the "nanostructure problem". In particular, bulk single crystals made of 102 Au atom NPs interconnected by organic molecules have been grown, the atomic structure of the crystals has been solved by traditional Bragg X-ray diffraction (XRD)[12,13] and so the positions of Au atoms in the NPs have been determined[31] with a low but acceptable resolution of 1.1 Å. This approach has not been pursued much further beyond. Non-diffraction based techniques such as, for example, Transmission Electron Microscopy (TEM),[32,33] Raman,[34] Extended X-ray Absorption Fine-Structure Spectroscopy (EXAFS)[35] and Nuclear Magnetic Resonance (NMR)[36] also have been used to study the atomic structure of NPs. However, due to their local structure only probe character, the techniques have not been able to solve the NP atomic structure but reveal some NP structural characteristics only. Thus, regardless of the sustained effort, no NP atomic structure has been solved, *i.e.* positions of all atoms in NPs have not been determined accurately yet.

Here we demonstrate that the NP atomic structure can be solved with success when both the technical and fundamental aspects of the "nanostructure problem" are addressed properly by (i) employing procedures not relying on sharp Bragg peaks in 1D diffraction patterns and, at the same time, (ii) completely abandoning the broken limits of Bravais lattice-based crystallography, respectively. For this purpose we employ a proper combination of a few widely available experimental and computational techniques. The techniques are described in the section below. As an example we solve the 3D atomic structure of 5 nm $Pd_xNi_{100-x}$ particles ($x = 26$, 56 and 88) explored for catalytic applications. The preparation of $Pd_xNi_{100-x}$ NPs is also described in the section below. The example is relevant since metallic NPs are known to adopt crystallographic and non-crystallographic type structures[37] each consistent with a number of different chemical patterns,[38] *i.e.* are non-trivial from a structural point of view. Note, other NP systems with non-trivial atomic structures could have been used to exemplify the approach to solving the "nanostructure problem" we demonstrate here since, as discussed below, it is not limited to NPs of particular chemistry, size or shape. Also note that we approach the "nanostructure problem" as a "finite size, extended free surface NP structure problem" leaving aside the cases of nanometer-size structural

fluctuations in bulk crystals[39-41] and glasses[42] since, usually, both are considered in terms of continuous atomic configurations subjected to 3D periodic boundary conditions.

## Experimental and computational techniques

**1.1. Sample preparation and characterization.** The synthesis of $Pd_xNi_{100-x}$ NPs ($x = 26$, 56 and 88) was based on reduction of Pd(II) and Ni(II) precursors in the presence of capping agents starting with dissolving palladium(II) acetylacetonate and nickel(II) acetylacetonate, mixed in a desired molar ratio, in benzyl ether, and adding 1,2-hexadecanediol as a reducing agent. After heating to 378 K in an $N_2$ atmosphere, oleic acid and oleylamine were added as capping agents. The purging in $N_2$ was discontinued and the solutions were further heated to 493 K with reflux for 0.5 h resulting in a complete change of their color to black. The solutions were then cooled down to room temperature and $Pd_xNi_{100-x}$ NPs with the desired Pd/Ni ratio precipitated out by adding ethanol and centrifugation. The NPs were dispersed in a hexane solvent, mixed with carbon black (XC-72) and sonicated in an ice bath for 3 h. Dry, carbon-supported NPs were obtained by removing the solvent and capping agents, including thermal processing (at 540 K) in an $O_2$ atmosphere for 30 min followed by processing (at 700 K) in an $H_2$ atmosphere for another 30 min.

The exact chemical composition of $Pd_xNi_{100-x}$ NPs was determined by inductively-coupled plasma optical emission spectroscopy (ICP-OES) using a Perkin Elmer 2000 DV ICP-OES instrument with the following parameters: 18.0 L $Ar_{(g)}$ per min plasma, auxiliary 0.3 L $Ar_{(g)}$ per min, a nebulizer of 0.73 L $Ar_{(g)}$ per min, 1500 W power and a peristaltic pump rate of 1.40 mL $min^{-1}$. For the measurements, several samples of each set of $Pd_xNi_{100-x}$ NPs were dissolved in concentrated aqua regia and diluted to concentrations in the range of 1 to 50 ppm. Elemental (Pd and Ni) concentrations were derived by measuring one or more (Pd or Ni) emission lines to check for interference and using multi-point calibration curves made from standards with concentrations from 0 to 50 ppm dissolved in the same acid matrix as the unknown. The standards were re-measured after analyzing 6 to 12 NP samples and the instrument was re-calibrated if the measured values were not within ±5% from the initial ones. The instrument reproducibility was determined using 1 mg $L^{-1}$ elemental solutions ensuring <±1 atomic % error for both Pd and Ni concentrations.

The size and morphology of $Pd_xNi_{100-x}$ NPs ($x = 26$, 56 and 88) were determined by TEM and confirmed by High-Angle Annular Dark-Field (HAADF)-scanning TEM (STEM) experiments. For the TEM measurements NP samples were diluted in hexane and drop cast onto carbon-coated copper grids followed by solvent evaporation in air at room temperature. TEM experiments were performed on a JEM-2200FS microscope operated at 200 kV. The microscope was fitted with an ultra-high-resolution (UHR) pole piece with a point resolution of 0.19 nm. Exemplary TEM and high-resolution (HR)-TEM images of $Pd_xNi_{100-x}$ NPs are shown in Fig. S2.†

A JEOL JEM 2100F TEM with a CEOS hexapole probe corrector attached was used to obtain HAADF-STEM images and Electron Energy Loss Spectroscopy (EELS) based elemental maps of $Pd_xNi_{100-x}$ NPs. The instrument was operated at 200 kV in STEM mode. The lens settings combined with the corrector tuning gave a spatial resolution of ~90 pm. HAADF images were taken at a collection angle larger than 50 mrad. Elemental maps of the NPs were obtained by EELS with both Pd $M_{4,5}$ and Ni $L_{23}$ peaks included. The beam convergence and angles for the EELS collection were set to be around 14 mrad and 40 mrad, respectively. Exemplary HAADF-STEM images of $Pd_{56}Ni_{44}$ NPs and EELS derived elemental maps of $Pd_xNi_{100-x}$ NPs ($x = 26$, 56 and 88) are shown in Fig. S3 and S6,† respectively.

The catalytic activity of dry $Pd_xNi_{100-x}$ NPs for CO oxidation was measured on a custom-built reaction system including a temperature-controlled reactor, gas flow/mixing/injection controllers, an online gas chromatograph (Shimadzu GC 8A) equipped with 5A molecular sieves, Porapak Q packed columns and a thermal conductivity detector. The gas environment included 0.5 vol% CO + 10 vol% $O_2$ balanced by $N_2$, 20 vol% $O_2$ balanced by $N_2$ and 15 vol% $H_2$ balanced by $N_2$. The catalytic activity in terms of the temperature at which 50% of CO conversion is achieved, $T_{1/2}$, is summarized in Fig. 7 introduced later on. Note that the lower the values of $T_{1/2}$ the better the catalytic activity.

**1.2. High-energy XRD experiments.** High-energy synchrotron XRD experiments were carried out at the 11-ID-C beamline of the Advanced Photon Source, Argonne. All NPs were measured with X-rays of energy 115 keV ($\lambda = 0.1080$ Å) up to wave vectors of 25 $Å^{-1}$. Carbon powder support alone was measured separately. For the measurements the samples were placed in glass capillaries. Experimental XRD patterns corrected for detector dead time, sample absorption, carbon support and background (air, *etc.*) scattering are shown in Fig. S1.† Note that these XRD patterns and so their Fourier counterparts, the atomic PDFs of Fig. 1, reflect ensemble averaged structural features of all $Pd_xNi_{100-x}$ NPs sampled by the X-ray beam in a way traditional powder XRD patterns reflect ensemble averaged structural features of all polycrystallites sampled by the X-ray beam in those experiments. Using ensemble averaged structural features to understand and explain ensemble averaged properties (catalytic, magnetic, optical, *etc.*) puts NP atomic structure–property exploration on the same footing. The XRD data of Fig. S1† were reduced to structure factors defined as:

$$S(q) = 1 + \left[ I^{coh}(q) - \sum c_i |f_i(q)|^2 \right] \Big/ \left| \sum c_i f_i(q) \right|^2, \quad (1)$$

where $c_i$ and $f_i(q)$ are the atomic concentration and X-ray scattering factor, respectively, for species of type $i$, that are Pd and Ni in our case. The structure factors were Fourier transformed into atomic PDFs as follows:

$$G(r) = \frac{2}{\pi} \int_{q=q_{min}}^{q_{max}} q[S(q) - 1]\sin(qr)dq, \quad (2)$$

where $q$ is the magnitude of the wave vector. The so-derived atomic PDFs are shown in Fig. 1. Note, by definition, $G(r) = 4\pi r(\rho(r) - \rho_o)$, where $\rho(r)$ and $\rho_o$ are, respectively, the local and average atomic number density and $r$ is the radial distance.[43] In this respect, atomic PDFs resemble Patterson
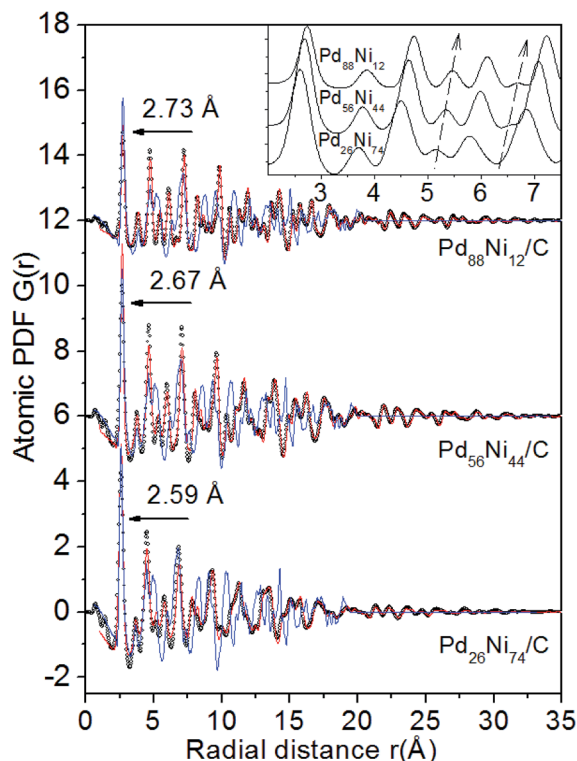
Fig. 1 Experimental (symbols), fcc-type crystallographic (lines in red) and icosahedral-type non-crystallographic (lines in blue) structure based PDFs for $Pd_xNi_{100-x}$ NPs. The position of the first peak in each experimental PDF is marked with a solid horizontal arrow. The low-$r$ part of the experimental PDFs (lines in black) is shown in the inset. Dashed arrows mark the evolution of subtle PDF features, $i.e.$ of subtle structural features of $Pd_xNi_{100-x}$ NPs, with Pd/Ni ratio.

functions widely used in traditional crystallography.[12] However, while Patterson functions peak at interatomic distances within a unit cell of a perfectly periodic, 3D infinite lattice, atomic PDFs do not imply any periodicity and so peak at distances separating all distinct pairs of atoms within the material under study, be it bulk single crystal, glass, polycrystalline powder or an ensemble of nanometer-size particles. Therefore, the experimental PDFs of Fig. 1 reflect nothing but distinct Ni–Ni, Ni–Pd and Pd–Pd pairs of atoms, immediate and all farther neighbors, within $Pd_xNi_{100-x}$ NPs. High-energy XRD and atomic PDFs have already been proven to be very efficient in studying the atomic-scale structure of nanometer-size materials, including metallic NPs.[20,21,24,44,45]

**1.3. Density functional theory (DFT) calculations.** DFT calculations were carried out using the Vienna *ab initio* simulation program (VASP) employing a plane-wave basis. The projector augmented-wave (PAW)[46] method was used to describe the electron-ion interactions. The Perdew–Burke–Emzerhof (PBE)[47] exchange correlation functional was used throughout the calculations. We explored 150-atom configurations of Pd and Ni species in appropriate proportions positioned inside a cubic super-cell applying periodic boundary conditions at constant volume for annealing, equilibrating, and cooling, and at zero pressure conjugate gradient (CG) for

relaxation. A time step of 2.5 fs was used in the calculations. First, the initially random 150-atom configurations were annealed at 2000 K, which is above the melting points of bulk Pd and Ni, for 30 ps. The configurations were then cooled down to 1000 K in 10 ps and equilibrated at this temperature for 30 ps. Finally, the configurations were cooled down to room temperature (300 K) at a cooling rate of 15 K $ps^{-1}$, subjected to an equilibration for 20 ps and fully relaxed to a local energy minimum at zero pressure. Analysis of the final configurations showed that Pd and Ni atoms are arranged on the vertices of a face-centered-cubic type lattice. DFT calculations under non-periodic boundary conditions were also carried out in the manner described above. Analysis of the resulting model atomic configurations showed that clusters of 150 Pd and Ni species may adopt both fcc-type crystallographic and icosahedral-type non-crystallographic atomic structures. The former, however, was found to be much more favourable than the latter because of its much lower energy ($-3.617$ eV per atom $vs.$ $-3.477$ eV per atom for fcc and icosahedral-type structures, respectively), $i.e.$ of its much higher stability. Nevertheless, as discussed below, not only fcc-type but also icosahedral-type atomic arrangements were considered and so tested as possible structure types for $Pd_xNi_{100-x}$ NPs.

**1.4. Classical molecular dynamics simulations.** The relatively simple but highly efficient, for modeling the atomic structure of metals and alloys, quantum corrected Sutton–Chen (Q-SC) potential,[48–50] as implemented in the computer code DL_POLY,[51] was employed in the classical molecular dynamics (MD) simulations. The Q-SC potential treats the atomic structure model energy, $U$, as a sum of two terms: an atomic pair potential $V(r_{ij})$ term and a local electron density ($\rho_i$) term[48–50] as follows:

$$U = \sum_i \left[ \sum_{j \neq i} \frac{1}{2} \varepsilon_{ij} V(r_{ij}) - c_i \varepsilon_{ij} (\rho_i)^{\frac{1}{2}} \right] \quad (3)$$

where

$$V(r_{ij}) = \left( \frac{a_{ij}}{r_{ij}} \right)^{n_{ij}} \quad (4)$$

and

$$\rho_i = \sum_{j \neq i} \left( \frac{a_{ij}}{r_{ij}} \right)^{m_{ij}} \quad (5)$$

Here the so-called length parameters $a_{ij}$ and $r_{ij}$ represent the lattice parameter and the distance between the $i^{th}$ and $j^{th}$ atoms from the model atomic configuration, respectively. The parameters $\varepsilon_{ij}$ and $c_i$ are used to scale the repulsive, $V(r_{ij})$, and attractive, $\rho_i$, energy terms, respectively, and $m$ and $n$ are positive integers such that $n > m$. The Q-SC potential parameters used in this study are presented in Table 1. They were verified by computing the cohesive energy of bulk Pd and Ni. MD simulations yielded cohesive energy values of 3.96 eV per atom and 4.66 eV per atom, respectively. These values compare very well with the experimental values of 3.89 eV and 4.44 eV, respectively.

| Metals | $m$ | $n$ | $\varepsilon$ (meV) | $a$ (Å) | $c$ |
|--------|-----|-----|---------------------|---------|-----|
| Ni     | 5   | 10  | 7.3767              | 3.5157  | 84.745  |
| Pd     | 6   | 12  | 3.2864              | 3.8813  | 148.205 |

As commonly accepted, the mixed $i$–$j$ atomic interactions were estimated as follows:

$$\varepsilon_{ij} = \sqrt{\varepsilon_i \varepsilon_j}, \ a_{ij} = \sqrt{a_i a_j}, \ m_{ij} = \frac{m_i + m_j}{2} \text{ and } n_{ij} = \frac{n_i + n_j}{2}. \quad (6)$$

Several structure models with the chemistry, size (approx. 4100 atoms) and shape (spherical) of $Pd_xNi_{100-x}$ NPs ($x = 26, 56$ and 88) studied here were explored. The models were optimized, i.e. their energy minimized, starting the MD simulations at 700 K accounting for the fact that the post-synthesis treatment of $Pd_xNi_{100-x}$ NPs was conducted up to that temperature only (see Section 1.1. above). The simulations were carried out under a canonical NVT ensemble using the velocity Verlet algorithm with a time step of 2 fs in the absence of periodic boundary conditions. Each of the models was equilibrated at 700 K for 200 ps, cooled down to room temperature (300 K) in steps of 50 K and again equilibrated for 50 ps. The energy of the so-optimized structure models was normalized per atom to facilitate comparison. As an example, MD optimized structure models for $Pd_{56}Ni_{44}$ NPs are shown in Fig. S4.†

**1.5.  FCC-type crystallographic and icosahedral-type non-crystallographic structure based computations of atomic PDFs.** Face-centered-cubic (fcc)-type crystallographic structure based atomic PDFs for $Pd_xNi_{100-x}$ NPs ($x = 26, 56$ and 88) were computed with the help of the program PDFgui.[25] Atomic PDFs for perfect fcc lattices were computed at first. Being identical all atoms had to be assigned a relevantly weighted average of the X-ray scattering power of Ni and Pd atoms. The δ-functions like PDF peaks, each corresponding to an atomic coordination sphere in a perfect fcc-type crystal structure, were then broadened by convolution with Gaussian functions to take into account the presence of thermal (Debye-Waller type) and static local atomic displacements in real NPs. Finally, parameters of the underlying fcc lattices, such as the length of the edge of their cubic unit cell, and parameters influencing the width of PDF peaks, such as average atomic thermal displacements, were adjusted so that the computed atomic PDFs approach the respective experimental data as close as possible. Icosahedral-type non-crystallographic structure based atomic PDFs for $Pd_xNi_{100-x}$ NPs ($x = 26, 56$ and 88) were computed in a similar manner except for the application of non-periodic boundary conditions and using the program DISCUS.[52] Results from the computations are shown in Fig. 1.

**1.6.  Hybrid reverse Monte Carlo simulations.** Hybrid reverse Monte Carlo (RMC) simulations were used to optimize several structure models for $Pd_xNi_{100-x}$ NPs ($x = 26, 56$ and 88). The starting atomic configurations were those used in the MD simulations. Atomic configurations already optimized in terms of energy by MD were also used as starting ones in the hybrid

RMC simulations. In general, hybrid RMC yielded virtually identical results for the cases when the respective starting atomic configurations had already been and not been MD optimized in terms of energy. The hybrid RMC simulations were easier and faster to conduct in the former than in the latter case.

In the spirit of traditional RMC simulations[53,54] the positions of atoms in a structure model being optimized were adjusted so as to minimize the difference between the model computed and the respective experimental atomic PDF. That difference appears as the first term in the function $\chi_D{}^2$ defined by eqn (8) introduced below. During the simulations Pd and Ni atoms were constrained to maintain as maximal (i.e. as close to 12) as possible coordination numbers. The constraint appears as the second term in the function $\chi_D{}^2$ defined by eqn (8). Also, Pd and Ni atoms were constrained not to come closer than preselected distances of the closest approach. The constraint appears as the third term in the function $\chi_D{}^2$ defined by eqn (8). The first constraint took into account the close packing nature of fcc-like atomic ordering identified, as described below, as a very plausible structure type for $Pd_xNi_{100-x}$ NPs. The second constraint reflected the fact that metal atoms may not approach each other much closer than the sum of the respective atomic radii $R_{ij}$. Radii of Pd and Ni atoms used here reflected the findings of DFT calculations and structure data mining carried out by us. A relatively new feature[55,56] turning the simulations into a hybrid between traditional RMC and MD was the optimization of the model's energy as described by the function $\chi_P{}^2$ defined by eqn (9) introduced below. The simultaneous minimization of the model's energy and the difference between the model computed and experimental PDF data is important since if the former or latter are done alone some inherent to NP's structural features (e.g. local structural disorder) may end up under or over-estimated, respectively. Model's energy was described by a pair-wise (Lennard-Jones type) potential defined as:

$$U = \varepsilon\left[\left(\frac{r_0}{r}\right)^{12} - 2\left(\frac{r_0}{r}\right)^6\right], \quad (7)$$

where $\varepsilon$ is the equilibrium energy and $r_o$ is the equilibrium distance between two like atoms. Values of $\varepsilon$ and $r_o$ for pure Pd and Ni were taken from literature sources.[57] The atomic cross-interactions (i.e. Pd–Ni) were described by $\varepsilon$ and $r_o$ parameters calculated as an arithmetic mean of the respective parameters for pure Pd and Ni. All in one, the hybrid RMC simulations aimed at the minimization of the residual function $\chi^2$ involving both $\chi_D{}^2$ and $\chi_P{}^2$ each defined as:

$$\chi_D{}^2 = \frac{\sum \left(G_i^{\text{exp}} - G_i^{\text{calc}}\right)^2}{\sigma_{G(r)}{}^2} + \frac{\sum \left(\text{CN}_i^{\text{des}} - \text{CN}_i^{\text{calc}}\right)^2}{\sigma_{\text{CN}}{}^2}$$
$$+ \frac{\sum \left(R_{ij}^{\text{des}} - R_{ij}^{\text{calc}}\right)^2}{\sigma_{R_{ij}}{}^2} \quad (8)$$

$$\chi_D{}^2 = \frac{\Delta U}{\sigma_{\Delta U}{}^2}. \quad (9)$$

Here $G_i^{\text{exp}}$ and $G_i^{\text{cal}}$ are calculated and experimental atomic PDFs for a given value of the real space distance $r_i$, $\text{CN}_i^{\text{des}}$ and

$CN_i^{cal}$ are preset, *i.e.* desired, and the model calculated first atomic coordination numbers, and $R_{ij}^{des}$ and $R_{ij}^{cal}$ are preset, *i.e.* desired, and the model calculated first atomic neighbour distances for $ij$ atomic pairs, respectively. The term $\Delta U$ reflects changes in the model's energy. Energy changes were triggered by adjusting atomic positions and swapping positions of nearby Pd and Ni atoms. The $\sigma$s in the denominators of eqn (8) and (9) are weighting factors achieving control over the relative importance of the individual terms in the residual function $\chi^2$ being minimized. In the course of simulations the values of $\sigma$ and the rate of swapping the positions of nearby Pd and Ni atoms were changed several times to increase the chances of finding the global minimum of the residual function $\chi^2$, instead of a local minimum. In the final stages of the simulations minimizing (i) the difference between experimental and calculated atomic PDF data and (ii) the energy of model atomic configurations was given preference over maintaining the preset CNs and distances of closest atomic approach. The latter though were never violated during the hybrid RMC simulations. The simulations were considered completed when no significant changes in the residual function $\chi^2$ were observed. The hybrid RMC simulations were done with the help of a new version[58] of the program RMC++. Structure models for $Pd_xNi_{100-x}$ NPs optimized by hybrid RMC are shown in Fig. 2 and 4. Note that the hybrid RMC described above is very much different from the so-called Empirical Potential Structure Refinement (EPSR) simulations which feature disordered but continuous atomic configurations subjected to 3D periodic boundary conditions.[59,60]

**1.7. Evaluation of the quality of structure models for $Pd_xNi_{100-x}$ NPs.** The quality of various MD and hybrid RMC optimized structure models for $Pd_xNi_{100-x}$ NPs ($x = 26, 56$ and 88) was evaluated by computing a reliability factor, $R_{wp}^{PDF}$, defined as:[25,44,61]

$$R_{wp}^{PDF} = \left\{ \frac{\sum w_i \left( G_i^{exp} - G_i^{calc} \right)^2}{\sum w_i \left( G_i^{exp} \right)^2} \right\}^{1/2} \quad (10)$$



**Fig. 3** Experimental (symbols) and model computed (lines in cyan) atomic PDFs for $Pd_{56}Ni_{44}$ NPs. The models are optimized by hybrid RMC simulations and feature three distinct chemical patterns shown in Fig. 2. The quality of each model is evaluated in terms of reliability indicator $R_{wp}^{PDF}$ (in cyan) described in Section 1.7. Atomic PDFs (lines in red) computed from the random alloy type structure solution for $Pd_{56}Ni_4$ NPs (see Fig. 4(b)) and its reliability indicator (in red) are also shown for comparison.



**Fig. 4** Atomic structure solutions for $Pd_xNi_{100-x}$ NPs ($x = 26$ (a), 56 (b) and 88 (c)) as optimized by hybrid RMC simulations. The solutions feature 4100 atom configurations with local fcc-like ordering and random alloy chemical patterns. Atomic PDFs computed from the solutions are matched against the respective experimental PDFs in Fig. 5. Pd atoms are in green and Ni atoms are in orange.



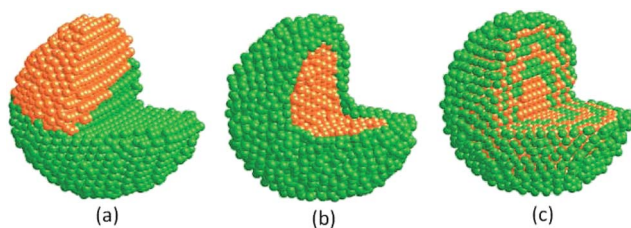**Fig. 2** Structure models for 5 nm $Pd_{56}Ni_{44}$ particles optimized by hybrid RMC simulations. The models feature 4100 atom configurations with local fcc-like ordering but distinct chemical patterns including Ni cluster-over-Pd cluster phase separated (a), $Ni_{core}$–$Pd_{shell}$ (b) and onion-like (c) patterns. The energy of respective structure models is −4.042 eV per atom, −4.049 eV per atom and −4.055 eV per atom, respectively. Atomic PDFs computed from the models are matched against the experimental PDF for $Pd_{56}Ni_{44}$ NPs in Fig. 3. Pd atoms are in green and Ni atoms are in orange.
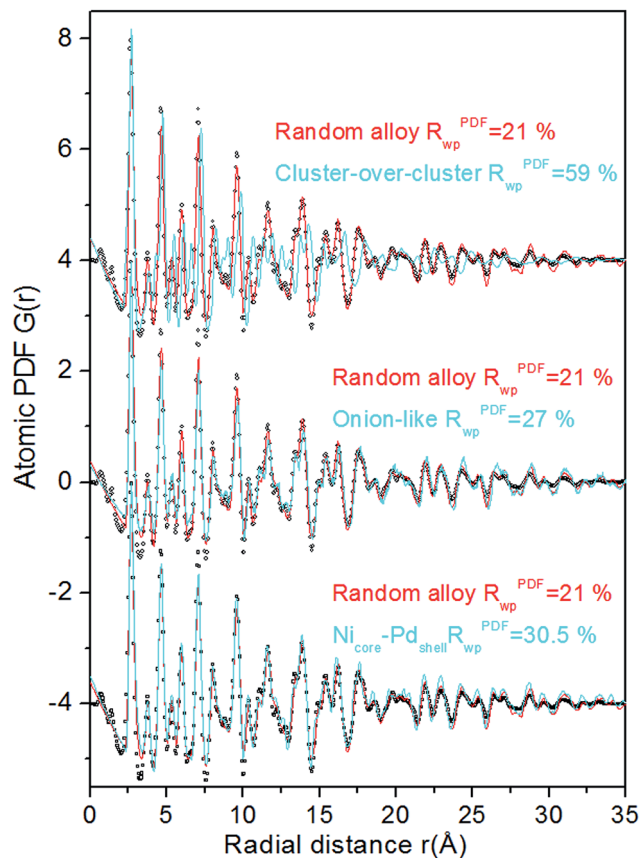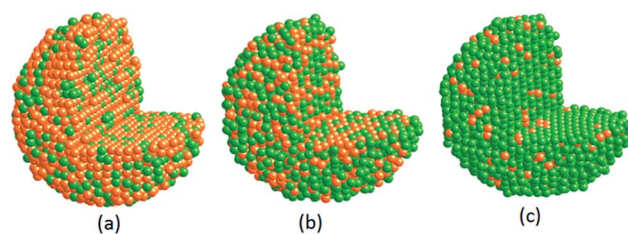
where $G^{exp}$ and $G^{calc}$ are the experimental and model computed atomic PDFs, respectively, and $w_i$ are weighting factors reflecting the experimental uncertainty of the individual $G^{exp}$ data points. Here $w_i$ were considered to be uniform which, as predicted by theory[62] and largely corroborated by experiment,[63] is a

reasonable approximation in the case of high quality $G^{exp}$ data such as ours. Note that $R_{wp}^{PDF}$ is conceptually very similar to the weighted profile agreement factor $R_{wp}^{PDF}$[64–66] used for evaluating how well a crystal structure model reproduces experimental powder diffraction data defined as:

$$R_{wp} = \left\{ \frac{\sum w_i \left( y_i^{exp} - y_i^{calc} \right)^2}{\sum w_i \left( y_i^{exp} \right)^2} \right\}^{1/2}, \qquad (11)$$

where $y_i^{exp}$ and $y_i^{calc}$ are, respectively, the observed and model calculated intensities at the step $i$ in the 1D polycrystalline powder diffraction pattern, and $w_i$ are weighting factors reflecting the quality of the experimental diffraction data. The typical values of $R_{wp}^{PDF}$ are, however, in the range of 15–30% (e.g. see Fig. 5) that appears somewhat high when compared to that of $R_{wp}$ values (usually less than 10%).[64–66] This mostly reflects the fact that atomic PDF analysis takes both Bragg-like features and the overall diffuse component of the experimental diffraction patterns into account while crystal structure determination from powder diffraction data focuses on sharp Bragg peaks alone. The inherently higher absolute values of $R_{wp}^{PDF}$, however, do not affect its functional purpose as a quantity allowing evaluation of the quality of NP structure models unambiguously.

## Results and discussion

To solve the atomic structure of $Pd_xNi_{100-x}$ NPs ($x = 26, 56$ and $88$) we chose to follow the logical sequence of steps involved in crystal structure determination on the basis of powder diffraction data. Accordingly, we considered the experimental diffraction data as obtained in reciprocal space at first. However, as can be seen in Fig. S1,† the experimental XRD patterns for $Pd_xNi_{100-x}$ NPs appear rather diffuse, a picture typical for nanometer-size materials. As mentioned above, it is this diffuse character of the 1D diffraction patterns for NPs that renders the well-established, sharp Bragg peak-based procedures for solving 3D atomic structures from 1D diffraction data inapplicable to NPs. Therefore, we considered the respective atomic PDFs instead since, as we[20,24,39,44,45] and others[21,25–27,29,40,41,61] have repeatedly shown, they lend themselves to convenient NP structure models' test and refinement. As can be seen in Fig. 1 peaks in the experimental PDFs decay to zero at distances shorter (~3.5 nm) than the physical size of $Pd_xNi_{100-x}$ NPs, which is ~5 nm as determined by TEM (see Fig. S2†) and confirmed by HAADF-STEM (see Fig. S3†), indicating the presence of non-negligible structural disorder. Such disorder is typical for NPs and, usually, is due to finite size and surface relaxation effects. Further inspection of the experimental PDF data reveals that PDF peaks smoothly change positions with Pd/Ni ratio (see the inset in Fig. 1). For example, the first peak in the PDF for $Pd_{26}Ni_{74}$, $Pd_{56}Ni_{44}$ and $Pd_{88}Ni_{12}$ NPs changes its position from 2.59 Å to 2.67 Å and then to 2.73 Å, respectively. The peak reflects the shortest atomic-pair distances, i.e. the radius of the first atomic coordination sphere in $Pd_xNi_{100-x}$ NPs. Clearly it evolves with the Pd/Ni ratio. New PDF features appear, shift in position and grow in intensity as well (the dashed arrows in the inset in Fig. 1). Evidently the

experimental PDFs are sensitive enough to capture both overall (e.g. the presence of disorder) and subtle (e.g. atomic-pair distances) features of the atomic structure of $Pd_xNi_{100-x}$ NPs, including the evolution of those features with Pd/Ni ratios.

Next, following the footsteps of crystal structure studies, we aimed at identifying the type of atomic structure exhibited by $Pd_xNi_{100-x}$ NPs. To do it we had to take into consideration the fact that, in spite of their very good sensitivity both to overall and fine features of the atomic structure of NPs, experimental atomic PDFs alone are not as fully amenable to an explicit identification of NP structure types as experimental Bragg diffraction patterns alone are in identifying crystal structure types.[12,43,65] Therefore, in the search of $Pd_xNi_{100-x}$ NPs' structure type we not only had to account for but also go beyond the experimental PDF data. In particular, encouraged by prior studies on monometallic NPs,[67] we employed DFT as a tool for investigating what types of atomic structures are likely to occur in the Pd–Ni system. Details of the DFT calculations are given in Section 1.3 above. DFT indicated that when Pd and Ni atoms are mixed together a fcc-type structure is most likely to occur. Icosahedral-type atomic arrangement, though much less favorable, also was found possible to occur. DFT, however, could not explore all types of atomic structures likely to be exhibited by 5 nm $Pd_xNi_{100-x}$ particles because of their relatively large size (about 4100 atoms). Therefore, additionally, we queried the experimentally determined atomic structures of bulk Pd–Ni crystals. All turned out to be of a fcc-type.[68] To verify the predictions of first-principles DFT and findings of prior structure studies on bulk Pd–Ni crystals we computed atomic PDFs for perfect, fcc-type crystallographic and icosahedral-type non-crystallographic structures, and compared the so-computed PDFs with the experimental PDFs. Details of the computations are given in Section 1.5 above. Results of the comparison are presented in Fig. 1. As can be seen in the figure, the fcc-type crystallographic structure based and experimental PDF data agree fairly well. On the other hand, the icosahedral-type non-crystallographic structure based and experimental PDF data largely disagree. The success of the former and failure of the latter model computations gave us confidence to consider fcc-type atomic arrangement as the most likely type of the atomic structure of $Pd_xNi_{100-x}$ NPs, and pursue that type further. Note, we could not just assume that the $Pd_xNi_{100-x}$ NPs' structure type should be similar to the bulk Pd–Ni crystals' structure type and casually pursue the latter without verification since prior studies have shown clearly[24,69–73] that the structure type of intrinsically non-3D periodic NP may be very different from the structure type of its bulk, intrinsically 3D periodic crystalline counterpart (also see Fig. S9†).

Once the structure type for $Pd_xNi_{100-x}$ NPs was identified and verified, relevant 3D structure models were generated by populating appropriate size (~5 nm per 4100 atoms) and shape (spherical) pieces of the fcc-type lattice with Pd and Ni atoms in pertinent proportions. The models were then optimized by minimizing their energy. The minimization was done by Molecular Dynamics (MD) simulations described in Section 1.4 above. MD optimized structure models for $Pd_{56}Ni_{44}$ NPs exhibiting two very different chemical patterns are shown in

Fig. S4.† In general, the MD optimized models reproduced the respective experimental PDF data reasonably well, except for the region of higher-$r$ values. This is exemplified in Fig. S5† where an atomic PDF computed from the MD optimized structure model for $Pd_{56}Ni_{44}$ NPs (see Fig. S4a†) features random alloy chemical pattern is compared with the respective experimental PDF data. Analysis of the MD optimized structure models revealed that the uniformly flat atomic planes terminating their surfaces were causing the misfit between the MD model computed and experimental PDFs at higher-$r$ values, *i.e.* at longer interatomic distances. Moreover, uniformly flat surfaces, *i.e.* an insignificant degree of surface structural disorder, were the opposite of what the high-resolution TEM images of $Pd_xNi_{100-x}$ NPs and the atomic resolution HAADF-STEM images of $Pd_{56}Ni_{44}$ NPs showed (see Fig. S2 and S3†). Evidently, MD optimized structure models did not reproduce well the positional disorder of surface atoms in $Pd_xNi_{100-x}$ NPs. Furthermore, MD optimized structure models with the same overall chemistry but distinct chemical patterns could not be unambiguously discriminated in terms of their minimized energy. For example, the energy of MD optimized structure models for $Pd_{56}Ni_{44}$ NPs featuring random alloy (Fig. S3a†) and $Ni_{core}$–$Pd_{shell}$ (S3b†) chemical patterns emerged to be −4.051 eV per atom and −4.052 eV per atom, respectively, *i.e.* came up pretty much about the same.

To obtain more precise and less ambiguous structure solution for $Pd_xNi_{100-x}$ NPs we carried out hybrid RMC simulations as described in Section 1.6 above. Among the explored chemical patterns were Ni cluster-over Pd cluster phase segregated, $Ni_{core}$–$Pd_{shell}$, onion-like and random alloy type patterns. These were suggested by previous experimental studies indicating that, depending on details of the synthesis and post-synthesis treatment, $Pd_xNi_{100-x}$ NPs may exhibit different chemical patterns with the $Ni_{core}$–$Pd_{shell}$ one occurring particularly often.[38] The latter may be expected since both the cohesive (4.66 eV per atom for Ni *vs.* 3.96 eV per atom for Pd) and surface (0.90 eV for Ni *vs.* 0.77 eV for Pd) energies for Ni are higher than those for Pd. As an example, hybrid RMC optimized structure models for $Pd_{56}Ni_{44}$ NPs featuring Ni cluster-over Pd cluster phase segregated, $Ni_{core}$–$Pd_{shell}$, onion-like and random alloy chemical patterns are shown in Fig. 2(a), (b), (c) and 4(b), respectively. The quality of the models was evaluated in terms of their energy and "reliability indicator" $R_{wp}^{PDF}$,[44,61,74] defined by eqn (10) in Section 1.7 above. The results of the evaluation are shown in Fig. 3. As can be seen in the figure the reliability indicators for the structure models featuring the Ni cluster-over Pd cluster, $Ni_{core}$–$Pd_{shell}$ and onion-like chemical patterns are significantly inferior to that of the structure model featuring the random alloy chemical pattern. Besides, the energy of the latter (−4.060 eV per atom) is lower than that of the former (−4.042 eV per atom for Ni cluster-over Pd cluster, −4.049 eV per atom for $Ni_{core}$–$Pd_{shell}$ and −4.055 eV per atom for onion-like models) rendering the random alloy type model the most accurate representation, *i.e.* solution, of the atomic structure of $Pd_{56}Ni_{44}$ NPs that could be achieved. Note that energy differences in the order of a few tens of meV per atom are typical for structure models differing in the degree of atomic ordering alone.[75–77]

Furthermore, the energy of the so solved atomic structure of $Pd_{56}Ni_{44}$ NPs (−4.06 eV per atom) is lower than that (−4.051 eV per atom) of the virtually identical MD optimized, random alloy type model of Fig. S4(a).† The former, however, reproduces the experimental PDF data much better than the latter (see Fig. S5†). Evidently, not only hybrid RMC optimizes the energy of NP structure models at least as good as MD, but also accounts for the experimental diffraction/PDF data to the fullest possible extent (compare the respective reliability indicators shown in Fig. S5†). According to the bond-angle distribution shown in Fig. S6† the randomly distributed Pd and Ni atoms in $Pd_{56}Ni_{44}$ NPs are fcc-like arranged locally. This is to be expected considering the similarity between the fcc-type structure based and experimental PDFs shown in Fig. 1. In a similar manner hybrid RMC optimized models featuring 4100 atom configurations with local fcc-like ordering and random alloy chemical patterns were found to be the most accurate representation of the atomic structure of $Pd_{26}Ni_{74}$ and $Pd_{88}Ni_{12}$ NPs that could be achieved. The so-solved atomic structure of $Pd_{26}Ni_{74}$ and $Pd_{88}Ni_{12}$ NPs is shown in Fig. 4(a) and (c), respectively, together with that of $Pd_{56}Ni_{44}$ NPs (Fig. 4(b)). The respective reliability indicators are summarized in Fig. 5. As can be seen in the figure the $R_{wp}^{PDF}$ values for the as-solved atomic structure of $Pd_xNi_{100-x}$ NPs ($x = 26$, 56 and 88) fall in the range of 18–22% which, as explained in Section 1.7 above, is considered a benchmark for success in atomic PDF-based structure studies. Thus, although the $Ni_{core}$–$Pd_{shell}$ pattern is considered as native for Pd–Ni NPs,[38] the $Pd_xNi_{100-x}$ NPs ($x = 26$, 56 and 88) studied here were found to be random nanoalloys. Independent confirmation of the random-alloy character of $Pd_xNi_{100-x}$ NPs ($x = 26$, 56 and 88) came from supplementary HAADF-EELS experiments (see Section 1.1) carried out after the type of atomic structure of $Pd_xNi_{100-x}$ NPs was identified and verified, initial 3D models of the fcc-type structure found the most plausible generated, optimized, evaluated and ranked as described above. As can be seen in Fig. 6 the EELS elemental maps show a rather scattered distribution of Pd and Ni species across $Pd_xNi_{100-x}$ NPs ($x = 26$, 56 and 88) confirming their random alloy character.

From the positions of atoms in the 3D structure solutions shown in Fig. 4 precise knowledge of essential structural characteristics of $Pd_xNi_{100-x}$ ($x = 26$, 56 and 88) NPs such as, for example, distribution of different chemical species across the NPs, also known as partial atomic PDFs, average partial and total first atomic coordination distances and numbers (CNs) within the NPs and at the NP surface alone, *etc.*, can be obtained easily.[78] Note that these characteristics are inaccessible if the NP atomic structure is considered in terms of a unit cell of a perfectly periodic, infinite 3D lattice. Partial atomic PDFs for $Pd_xNi_{100-x}$ ($x = 26$, 56 and 88) NPs are shown in Fig. S7.† The position of the first peak in a partial PDF corresponds to the respective first atomic neighbor distance.

Data in Fig. S7† show that the first neighbor Ni–Ni distance, reflecting the diameter/size of Ni atoms, increases from 2.50 Å to 2.53 Å and then to 2.55 Å with increasing the relative amount of Pd from 26% to 56% and then to 88%, respectively. The size of Pd atoms also increases with Pd concentration from 2.68 Å to 2.72 Å and then to 2.74 Å, respectively. Note that the size of Ni
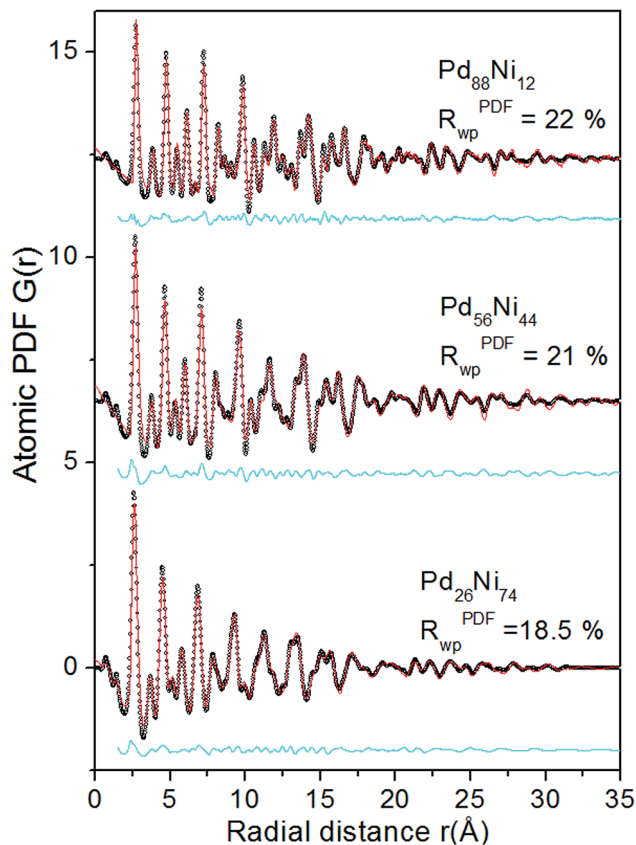
Fig. 5 Experimental (symbols) and atomic structure solutions derived (solid lines in red) atomic PDFs for $Pd_xNi_{100-x}$ NPs ($x$ = 26, 56 and 88). The structure solutions are shown in Fig. 4(a)–(c), respectively. The quality of each structure solution is evaluated in terms of reliability indicator $R_{wp}^{PDF}$, described in Section 1.7. The values of $R_{wp}^{PDF}$ are rather low which is typical for structure solutions of very good quality. The so-called difference line plots are given beneath each dataset as shifted by a constant for clarity (lines in cyan). The plots represent the difference between the full profiles of the respective experimental and structure solution derived atomic PDFs. All three difference plots exhibit low-amplitude, high-frequency ripples only providing extra evidence[32–34] for the very good quality of the NP atomic structure solutions provided by the approach for solving the "nanostructure problem" demonstrated here.



Fig. 6 HAADF-STEM images (up) and EELS elemental maps (down) for single $Pd_xNi_{100-x}$ NPs with $x$ = 26 (a), $x$ = 56 (b) and $x$ = 88 (c). Elemental maps show rather scattered distribution of Pd and Ni species across the NPs reflecting their random-alloy character. Ni species distribution is in red and Pd species distribution is in green.

and Pd atoms in bulk Ni and Pd is 2.48 Å and 2.75 Å, respectively. Evidently the size of Ni atoms in $Pd_xNi_{100-x}$ NPs approaches that in bulk Ni at low ($x$ = 26) Pd concentration. With increasing the relative amount of Pd the size of Ni atoms in $Pd_xNi_{100-x}$ NPs increases well beyond that in bulk Ni. The size of Pd atoms in $Pd_xNi_{100-x}$ NPs approaches that in bulk Pd at low Ni concentration. With increasing the relative amount of Ni the size of Pd atoms in $Pd_xNi_{100-x}$ NPs decreases well beyond that in bulk Pd. The observed expansion of Ni and shrinking of Pd atoms indicate redistribution of charge in $Pd_xNi_{100-x}$ NPs with changing the Pd/Ni ratio.

As postulated by the theory of chemical bonding of Pauling[79–81] metal atoms receiving extra charge would become smaller in size due to the increased attraction of the electron cloud by the nuclei while ones loosing charge would become larger. Pa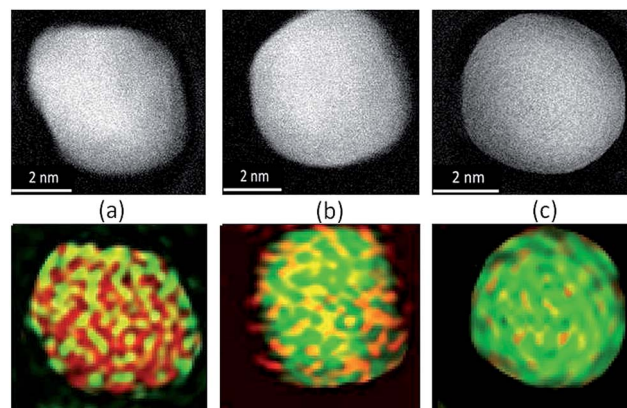uling has also proposed that charge transfer on the metallic atom-pair bond on alloying would be proportional to the electronegativity difference between the respective atoms, for maintaining electroneutrality. For reference, the electronegativity of Pd is 2.28 and that of Ni is 1.9 suggesting charge transfer toward Pd, i.e. increasingly smaller Pd atoms with increasing Ni concentration and progressively larger Ni atoms with increasing Pd concentration, which is exactly what we observe. Charge redistribution may influence the catalytic properties of metallic NPs considerably.[3] Hence, precise knowledge of it may prove rather useful for the understanding of these properties.

The average partial Pd–Pd and Pd–Ni CNs and the average total first CN inside $Pd_{56}Ni_{44}$ NPs, derived from the respective atomic structure solution (see Fig. 4b), are 6.2, 5.2 and 11.5, respectively. The similarity between the average Pd–Pd and Pd–Ni CNs reflects the random alloy character of the atomic structure of $Pd_{56}Ni_{44}$ NPs. On the other hand, the relatively large value of total CN reflects its closely packed nature. The average partial Pd–Pd and Pd–Ni CNs and the average total first CN involving atoms at the surface of $Pd_{56}Ni_{44}$ NPs only reduce to 4.04, 3.4 and 7.1, respectively, reflecting the incomplete coordination spheres of atoms at the NP surface. The distribution of the total first CNs for atoms at the $Pd_{56}Ni_{44}$ NP surface only, as obtained from the respective atomic structure solution, is shown in Fig. S8.† It is rather broad showing 9- and 8-fold coordinated atoms, indicative of close packed, planar-type atomic configurations, as well as 7- to 4-fold coordinated atoms, indicative of terraces, edges and sharp corners at the NP surface. Such a variety of atomic configurations occurs when NPs exhibit non-negligible surface structural disorder which is exactly what the high-resolution TEM and atomic resolution HAADF-STEM images (see Fig. S2 and S3†) as well as the enhanced decay of the experimental PDFs at higher-$r$ values (see Fig. 1 and the inset in S5†) indicate. Low coordinated surface atoms are known to enhance the catalytic activity of metallic NPs[82,83] for some reactions. However, the opposite may happen when the number of very low coordinated surface atoms, in

particular that of 4-fold and 5-fold coordinated atoms, exceeds some critical threshold.[84] Hence, precise knowledge of the first CNs for surface atoms in metallic NPs also may prove rather useful for the understanding of their catalytic properties.

Fig. 7 illustrates how this pertains to $Pd_xNi_{100-x}$ NPs, *i.e.* how precise knowledge of the particular structural characteristics of $Pd_xNi_{100-x}$ NPs discussed above can help understand better and so design a rational strategy for further improving their catalytic properties. As can be seen in the figure the catalytic activity of $Pd_xNi_{100-x}$ NPs appears enhanced when (i) surface Pd atoms and their first neighbors pack closer, (ii) the NP surface becomes less corrugated, and (iii) the distance between nearby Pd and Ni atoms at the NP surface elongates. Therefore,
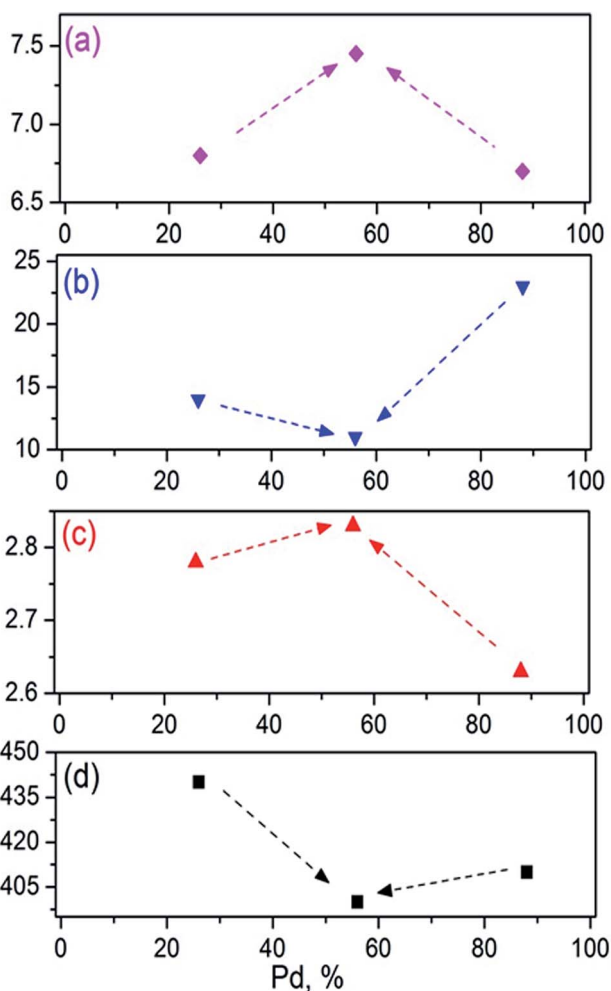
coordinated effort aiming at enhancement of (i) to (iii) is very likely to be a successful strategy for further improving the catalytic activity of $Pd_xNi_{100-x}$ NPs for CO oxidation. The effort may involve fine tuning of the parameters of NP synthesis/post-synthesis treatment[20] and/or others.

Precise knowledge of the atomic-scale structure of metallic NPs may be important not only for the understanding of their catalytic but also magnetic, optical and bio-medical properties. For example, positions of atoms in a thin slab of the realistically rugged (*e.g.* see Fig. S8†) and curved (*e.g.* see Fig. 4) surface of a precisely determined 3D structure of NPs may constitute a basis for accessing docking of proteins to the surface of these NPs that is much better than the commonly used approximations featuring slabs made of flat atomic planes of regular crystalline lattices.[85]

## Conclusions

In conclusion, we demonstrate an approach to solving the "nanostructure problem" including 6 coherent steps. The steps, (i) to (vi), are summarized below and, for methodological clarity, compared with those involved in the approach for solving crystal structures from powder diffraction data.[17,63–65] The comparison is fair since both approaches rely on 1D diffraction datasets obtained from ensembles of entities with largely identical atomic-scale structures and some dispersity in sizes and shapes. Step (i): the ensemble averaged NP chemical composition, size and shape should be precisely determined since all three are an integral part of NP atomic structure solution. In particular, the former takes into account the common dependence of the atomic-scale structure on chemical composition (*e.g.* see the inset in Fig. 1) and the latter two – the fact that atomic-scale structure, size, shape and properties of nanometer-size materials are intimately coupled.[18,66–70,80,82,83] Understandably, the smaller the dispersity in the NP size and shape the smaller the danger of ending up with a biased (*e.g.* toward a particular NP size/shape) solution for the "nano-structure problem". Powder diffraction studies too require prior knowledge of crystallite's chemical composition. Prior knowledge of the crystallite's size and shape is not necessarily needed since, typically, a crystal atomic structure does not depend on the crystal's size and shape.[12,17,64,65] Step (ii): very good quality diffraction data have to be collected to high wave vectors so that the respective atomic PDFs are with high real-space resolution.[43,44,61] Data can be collected from NPs that are compacted, *i.e.* self-supporting,[28,86] dispersed in solid, as is the case with carbon supported $Pd_xNi_{100-x}$ NPs studied here, or in a soft (*e.g.* polymeric)[24] matrix, in solution,[45,87] subjected to a reactive gas atmosphere and elevated temperature[20] or others. High wave vectors can be reached by employing high-energy synchrotron X-rays, as done here, neutron[26] or electron diffraction.[88] A combination of X-ray, neutron and/or electron diffraction may be very useful in the case of multicomponent NPs because of the different scattering power of atoms for X-rays, neutrons and electrons.[13] Chemistry specific PDFs obtained by resonant high-energy synchrotron XRD[73] may be added to the mix. Note that crystal structure studies based on traditional powder diffraction



Fig. 7 (a) Total first CN for Pd atoms ($CN_{Pd-Pd}$ + $CN_{Pd-Ni}$) at the surface of $Pd_xNi_{100-x}$ NPs. The CN is used here as an indicator of the closeness/density of the atomic packing around surface Pd atoms; (b) excessive corrugation of the $Pd_xNi_{100-x}$ NP surface estimated in terms of the relative % of surface atoms with the total first CN of 4 and 5; (c) distance (in Å) between nearby Pd and Ni atoms at the surface of $Pd_xNi_{100-x}$ NPs; and (d) experimental catalytic activity of $Pd_xNi_{100-x}$ NPs for CO oxidation reaction in terms of the temperature $T_{1/2}$ (in K) at which 50% CO conversion is achieved. Details of the catalytic activity measurements are given in Section 1.1 Note that data shown in (a)–(c) are derived from the respective atomic structure solutions shown in Fig. 4.

also rely on X-ray and/or neutron and/or resonant XRD[89] data. Powder diffraction, however, targets achieving high resolution in reciprocal[17,64–66] and not in real space. Hence, typical powder diffraction patterns do not extend to high wave vectors. Step (iii): the type of atomic structure of NPs studied should be identified with a high degree of certainty. Assuming that it ought to be similar to the structure type of a bulk material of identical chemistry and so considering that the structure type only may turn into a roadblock to solving the "nanostructure problem" as exemplified in Fig. S9.† Powder diffraction studies may need nothing but sharp Bragg peaks to search for and identify the crystal structure type unambiguously since that type must comply with both the translational and local symmetry elements of one out of 230 in number only, so-called, space groups.[13,17,64,65] Constraints imposing strict 3D periodicity and uniformity may not be *a priory* applied to NP atomic structures rendering the number of possible NP structure types much larger than that of the possible crystal structure types. Hence, extra to the experimental PDF data clues, including sound chemical intuition,[90] may be needed to help search for and identify NP structure types in a self-consistent and not erratic manner. As shown here, a combination of first-principles DFT predictions with structure data mining aimed at pinpointing likely NP structure type(s) followed by verification based on experimental PDF data may do a very good job. Other approaches, in particular MD simulations based, may be equally successful. Step (iv): 3D model(s) of the NP structure type identified and the actual NP chemistry, size and shape, precisely determined in step (i), are to be generated next. This can be done semi-manually,[24,45,70,76] as done here, or largely automatic.[26,90] For comparison, 3D structure models for crystals feature relatively small size unit cells of Bravais lattices containing pertinent atomic species occupying positions consistent with the symmetry elements of the given space groups.[17,64,65] Step (v): the initial NP structure model(s) have to be optimized to the fullest possible extent. If the optimization targets minimization of model's energy alone, as done by classical MD, the outcome may not reflect well some structural characteristics inherent to NPs such as, for example, the presence of NP surface relaxation & structural disorder (*e.g.* see Fig. S5†). One of the obvious reasons is that, usually, model's energy is described with potentials/force fields developed and tested on *ab initio* or experimental data for bulk and not nanometer-size materials. Nevertheless, structure models with optimized energy alone still can be very useful in exploring likely NP structure types,[27] elucidating NP structure trends[91] and in providing starting points for subsequent NP atomic structure optimization guided by experimental data such as, for example, atomic PDF data. Indeed we found that when RMC-type model structure optimization starts from atomic configurations with energy already optimized by MD and not from scratch, NP structure solutions are easier and faster to arrive at. Techniques such as hybrid RMC appear more successful than MD alone because not only they minimize both model's energy and the difference between model computed and experimental PDF data simultaneously but also can accommodate various NP atomic structure relevant constraints such as interatomic distances of the closest

approach, total or partial coordination numbers, bond angles, distribution of chemical species across the NPs, and others. Constraints may be based entirely on sound chemical intuition[90] and/or on experimental data from complementary local structure probe techniques such as Raman, EXAFS and NMR. Atomic structure-relevant constraints of the type described above also are used in the optimization of crystal structure models. That optimization, however, aims exclusively at minimizing the difference between model computed and experimental diffraction data in reciprocal space, paying particular attention to sharp Bragg peaks.[17,64,66] Furthermore, usually, the energy of crystal structure models is not optimized since positions of atoms in crystals are constrained heavily by symmetry elements of the respective space group(s).[12,13] The energy of NP structure models has to be optimized since positions of atoms in NPs are much less constrained. Step (vi): the quality of optimized NP structure model(s) should be evaluated and model(s) ranked accordingly. For this purpose, a suitable indicator of model's quality such as, for example, the reliability indicator $R_{wp}^{PDF}$ defined by eqn (10) is to be used. Model's energy may be considered as well, though differences in energy may not necessarily be as obvious as differences in $R_{wp}^{PDF}$ values (compare differences in energy between models in Fig. 2 with differences in the respective $R_{wp}^{PDF}$ values in Fig. 5). An NP structure model with (i) well optimized energy and (ii) the highest possible quality, *i.e.* showing a very low $R_{wp}^{PDF}$ value, can be considered as a precisely determined (*i.e.* solved) atomic structure of the NPs under study. Furthermore, to be considered as structure solution, that model should be consistent with all other NP structure-sensitive data possibly available (*e.g.* CNs and bond lengths determined by local structure prober techniques) and, when applicable, meet proven in practice criteria such as, for example, bond valence sums.[92] Quality of crystal structure models optimized against powder diffraction data is evaluated and models ranked in a very similar way.[17,64,66]

The quality of the solved NP atomic structure may be cross checked further by, for example, inspecting the way it reproduces very fine details in the experimental diffraction data both in reciprocal/$S(q)$ space (see Fig. S10†) and real/PDF space (see the "difference line plots" in Fig. 5). The representativeness of the solved NP atomic structure, *i.e.* how well it reflects the atomic structure of individual entities of the ensemble of NPs studied, may also be cross-checked using techniques sensitive to single NPs such as, for example, high-resolution TEM, HAADF-STEM-EELS, as done here, or others.

As our present and prior studies show very realistic 3D structure models for NPs with various sizes, shapes and chemistry are fairly easy to generate and verify against experimental atomic PDFs. Examples include models of 3 to 30 nm in size and spherical in shape metallic NPs of fcc, *i.e.* crystallographic,[38] or icosahedral, *i.e.* non-crystallographic, type structures,[71] 8 to 25 nm in size and spherical in shape alloy NPs of metallic glass, *i.e.* amorphous type structures,[93] 2 to 6 nm in size and spherical in shape core–shell quantum dots,[94] metal oxide hollow tubes with inner and outer diameters of ∼10 and 20 nm, respectively,[70] metal oxide solid tetrapods with ∼2 nm wide and 11 nm long arms,[95] 9 nm in size and snow-flake-like in shape all

organic ($C_{2616}H_{6048}N_{432}$) NPs,[90] often referred to as polymer mimics of proteins, 2 to 14 nm in size and spherical in shape semiconductor NPs of quite open, diamond-type structures,[96] and others. These examples indicate that the approach described here is broadly applicable. Last but not the least the approach can be implemented straightway since it relies on a combination of widely available experimental and computational techniques. As such it has all the qualities needed to become a road map (see Fig. S11†) for solving the "nanostructure problem".[11]

A successful approach for optimizing, evaluating and ranking of crystal structure models and so ultimately solving the crystal atomic structure on the basis of 1D Bragg diffraction data was first demonstrated in the mid-1960s.[97,98] However, it took about 30 years for the approach to be more-or-less automated by developing software packages incorporating its most important steps in a convenient way.[17,64,99] About that time clones of the approach streamlined for crystalline materials of particular chemistry (*e.g.* all organic) and structure type (*e.g.* molecular) were developed as well.[100] Some time may also be needed to streamline, automate and clone the approach for truly solving and not merely approximating NP atomic structures on the basis of 1D atomic PDF data demonstrated here. Nevertheless, even as it is right now, the approach can challenge the "nanostructure problem" with marked success.

## Acknowledgements

## References

1  P. Alivisatos, *Endeavour*, 1977, **21**, 56.
2  C. Höppener, Z. J. Lapin, P. Bharadwaj and L. Novotny, *Phys. Rev. Lett.*, 2012, **109**, 017402.
3  B. R. Cuenya, *Thin Solid Films*, 2010, **518**, 3127.
4  D. Beydoun, R. Amal, G. Low and S. McEvoy, *J. Nanopart. Res.*, 1999, **1**, 439.
5  R. R. Arvizo, S. Bhattacharyya, R. A. Kudgus, K. Giri, R. Bhattacharya and P. Mukherjee, *Chem. Soc. Rev.*, 2012, **41**, 2943.
6  N. S. Wigginton, K. L. Haus and M. F. Hochella Jr, *J. Environ. Monit.*, 2007, **9**, 1306.
7  M. Reich, S. Utsunomiya, S. E. Kesler, L. Wang, R. C. Ewing and U. Becker, *Geolog. Soc. Am.*, 2006, **34**, 1033.
8  G. A. Waychunas, C. S. Kim and J. F. Banfield, *J. Nanopart. Res.*, 2005, **7**, 409.
9  H. P. Erickson, *Biol. Proced. Online*, 2009, **11**, 32.
10  L. Slabinski, L. Jaroszewski, A. P. C. Rodrigues, L. Rychlewski, I. A. Wilson, S. A. Lesley and A. Godzik, *Protein Sci.*, 2007, **16**, 2472.
11  S. J. L. Billinge and I. Levin, *Science*, 2007, **316**, 561.
12  C. Giacovazzo, *Fundamentals of Crystallography*, Oxford University Press, 1992.
13  T. Hahn, *International Tables for Crystallography*, Kluwer Academic Publishers, Boston, 2002.
14  R. B. Von Dreele, P. W. Stephens, G. D. Smith and R. H. Bllessing, *Acta Crystallogr., Sect. D: Biol. Crystallogr.*, 2000, **56**, 1549.
15  J. Wang, B. H. Toby, P. L. Lee, L. Ribaud, S. M. Antao, C. Kurtz, M. Ramanathan, R. B. Von Dreele and M. A. Beno, *Rev. Sci. Instrum.*, 2008, **79**, 085105.
16  F. Izumi and K. Momma, *Solid State Phenom.*, 2007, **130**, 15; C. J. Gilmore, K. Shankland and G. Bricogne, *Proc. R. Soc. London, Ser. A*, 1993, **442**, 97.
17  V. K. Pecharsky and P. Y. Zavalij, *Fundamentals of Powder Diffraction and Structural Characterization of Materials*, Kluwer Academic Publishers, 2003.
18  S. G. Sun, *Prog. Solid State Chem.*, 2007, **35**, 1.
19  W. J. Huang, R. Sun, J. Tao, L. D. Menard, R. G. Nuzzo and J. M. Zuo, *Nat. Mater.*, 2008, **7**, 308.
20  V. Petkov, S. Shan, P. Chupas, J. Yin, L. Yang, J. Luo and C. J. Zhong, *Nanoscale*, 2013, **5**, 7379.
21  B. Gilbert, F. Huang, H. Zhang, G. A. Waychunas and J. F. Banfield, *Science*, 2004, **305**, 651; D. Marks, *Rep. Prog. Phys.*, 1994, **57**, 603.
22  Y.-C. Hsieh, Y. Zhang, D. Su, V. Volkov, R. Si, L. Wu, Y. Zhu, W. An, P. Liu, P. He, S. Ye, R. R. Adzic and J. X. Wang, *Nat. Commun.*, 2013, **4**, 2466.
23  C. Antoniak, M. Spasova, A. Trunova, K. Fauth, F. Wilhelm, A. Rogalev, J. Minar, H. Ebert, M. Farle and H. Wende, *J. Phys.: Condens. Matter*, 2009, **21**, 336002.
24  V. Petkov, N. Bedford, M. R. Knecht, M. G. Weir, R. M. Crooks, W. Tang, G. Henkelman and A. Frenkel, *J. Phys. Chem. C*, 2008, **112**, 8907.
25  L. Farrow, P. Juhás, J. W. Liu, D. Bryndin, E. Božin, J. Bloch, Th. Proffen and S. J. L. Billinge, *J. Phys.: Condens. Matter*, 2007, **19**, 335219.
26  K. Page, T. C. Hood, T. Proffen and R. B. Neder, *J. Appl. Crystallogr.*, 2011, **44**, 327.
27  H. Zhang, B. Chen, J. F. Banfield and G. A. Waychunas, *Phys. Rev. B: Condens. Matter Mater. Phys.*, 2008, **78**, 214106.
28  B. Gilbert, J. J. Erbs, R. Lee Penn, V. Petkov, D. Spagnoli and G. A. Waychunas, *Am. Mineral.*, 2013, **98**, 1465.
29  P. Juhas, D. M. Cherba, P. M. Duxbury, W. F. Punch and S. J. L. Billinge, *Nature*, 2006, **440**, 655.
30  M. J. Cliffe and L. Godwin, *J. Phys.: Condens. Matter*, 2013, **25**, 454218.
31  P. D. Jadzinsky, G. Calero, C. J. Askerson, D. A. Bushnell and R. D. Kornberg, *Science*, 2007, **318**, 430.
32  M. J. Walsh, K. Yoshida, A. Kuwabara, M. L. Pay, P. L. Gai and E. D. Boyes, *Nano Lett.*, 2012, **12**, 2027.
33  C. Cui, L. Gan, M. Heggen, S. Rudi and P. Strasser, *Nat. Mater.*, 2013, **12**, 765.
34  A. Kassiba, M. Makowska-Janusik, J. Boucle, J. F. Bardeau, A. Bulou and N. Herlin-Boime, *Phys. Rev. B: Condens. Matter Mater. Phys.*, 2002, **66**, 155317.
35  A. Frenkel, *Z. Kristallogr.*, 2007, **222**, 605.
36  A. Arnold, V. Terskikh, Q. Ying Li, R. Naccache, I. Marcotte and J. A. Capobianco, *J. Phys. Chem. C*, 2013, **117**, 25733.
37  D. Marks, *Rep. Prog. Phys.*, 1994, **57**, 603.

38 R. Ferrando, J. Jellinek and R. L. Johnston, *Chem. Rev.*, 2008, **108**, 845.

39 S.-J. Hwang, V. Petkov, K. K. Rangan, S. Shastri and M. G. Kanatzidis, *J. Phys. Chem. B*, 2002, **106**, 12453.

40 L. Jiang, D. C. Mitchell, W. Dmowski and T. Egami, *Phys. Rev. B: Condens. Matter Mater. Phys.*, 2013, **88**, 014105.

41 K. M. Ø. Jensen, E. S. Boźin, C. D. Malliakas, M. B. Stone, D. Mark, M. G. Kanatzidis, S. M. Shapiro and S. J. L. Billinge, *Phys. Rev. B: Condens. Matter Mater. Phys.*, 2012, **86**, 085313.

42 T. Campbell, R. K. Kalia, A. Nakano, F. Shimojo, K. Tsuruta, P. Vashishta and S. Ogata, *Phys. Rev. Lett.*, 1999, **82**, 4018.

43 P. K. Klug and L. E. Alexander, *X-Ray Diffraction Procedures: for Polycrystalline and Amorphous Materials*, John Wiley & Sons Inc., New York, 2nd edn, 1974.

44 V. Petkov, Pair Distribution Function Analysis, in *Characterization of Materials*, Wiley, 2012, pp. 1361–1372.

45 V. Petkov, Y. Peng, G. Williams, B. Huang, D. Tomalia and Y. Ren, *Phys. Rev. B: Condens. Matter Mater. Phys.*, 2005, **72**, 195402.

46 P. E. Blochl, *Phys. Rev. B: Condens. Matter Mater. Phys.*, 1994, **50**, 17953.

47 J. P. Perdew, K. Burke and M. Ernzerhof, *Phys. Rev. Lett.*, 1996, **77**, 3865.

48 M. W. Finnis and J. E. Sinclair, *Philos. Mag. A*, 1984, **50**, 45.

49 A. P. Sutton and J. Chen, *Philos. Mag. Lett.*, 1990, **61**, 139.

50 Y. Kimura, Y. Qi, T. Cagin and W. Goddard III, *MRS Symp. Ser.*, 1999, **554**, 43.

51 W. Smith, W. C. Yong and P. M. Rodger, *Mol. Simul.*, 2002, **28**, 86.

52 Th. Proffen and R. B. Neder, *J. Appl. Crystallogr.*, 1999, **32**, 838.

53 R. L. McGreevy and L. Pusztai, *Mol. Simul.*, 1998, **1**, 359.

54 V. Petkov and G. Junchov, *J. Phys.: Condens. Matter*, 1994, **6**, 10885.

55 T. D. Bennet, A. L. Goodwin, M. T. Dove, D. A. Keen, M. G. Tucker, E. R. Barney, A. K. Soper, E. G. Bithel, J.-C. Tan and A. K. Cheetham, *Phys. Rev. Lett.*, 2010, **104**, 115503.

56 N. P. Funnel, M. T. Dove, A. L. Goodwin, S. Parsons and M. G. Tucker, *J. Phys.: Condens. Matter*, 2013, **45**, 452404.

57 H. Heinz, R. A. Vaia, B. L. Farmer and R. R. Naik, *J. Phys. Chem. C*, 2008, **112**, 17281.

58 O. Gereben and V. Petkov, *J. Phys.: Condens. Matter*, 2013, **25**, 454211.

59 A. K. Soper, *Phys. Rev. B: Condens. Matter Mater. Phys.*, 2005, **72**, 104204.

60 A. K. Soper, K. Page and A. Llobet, *J. Phys.: Condens. Matter*, 2013, **25**, 454219.

61 T. Egami and S. J. L. Billinge, *Underneath the Bragg Peaks: Structural Analysis of Complex Materials*, Pergamon Press, Elsevier Ltd., New York, 2003.

62 B. H. Toby and T. Egami, *Acta Crystallogr., Sect. A: Found. Crystallogr.*, 1992, **48**, 336.

63 L. B. Skinner, C. Huang, D. Schlesinger, L. G. M. Petterson, A. Nillson and C. J. Benmore, *J. Chem. Phys.*, 2013, **138**, 074506.

64 W. I. F. David, K. Shakland, L. B. McCusker, and C. Baerlocher, *Structure Determination from Powder Diffraction*, Oxford University Press., Oxford, 2002.

65 R. J. Hill and R. X. Fischer, *J. Appl. Crystallogr.*, 1990, **23**, 462.

66 B. H. Toby, *Powder Diffr.*, 2006, **21**, 67.

67 O. Lopez-Acevedo, J. Akola, R. L. Whetten, H. Gronbeck and H. Hakkinen, *J. Phys. Chem. C*, 2009, **113**, 5035.

68 L. R. Bidwell, *Acta Crystallogr.*, 1964, **17**, 1473.

69 S. K. Pradhan, Y. Mao, S. S. Wong, P. Chupas and V. Petkov, *Chem. Mater.*, 2007, **19**, 6180.

70 V. Petkov, P. Y. Zavalij, S. Lutta, M. S. Whittingham, V. Parvanov and S. Shastri, *Phys. Rev. B: Condens. Matter Mater. Phys.*, 2004, **69**, 085410.

71 V. Petkov, Y. Lee, S. Sun and Y. Ren, *J. Phys. Chem. C*, 2012, **116**, 26668.

72 V. Petkov, S. J. L. Billinge, J. Hesing and M. G. Kanatzidis, *J. Am. Chem. Soc.*, 2000, **122**, 11571.

73 V. Petkov, R. Loukrakpam, L. Yang, B. N. Wanjala, J. Luo, C.-J. Zhong and S. Shastri, *Nano Lett.*, 2012, **12**, 4289.

74 V. B. H. Toby and T. Egami, *Acta Crystallogr., Sect. A: Found. Crystallogr.*, 1992, **48**, 336.

75 B. Prasai, G. Chen and D. A. Drabold, *Appl. Phys. Lett.*, 2013, **102**, 041907.

76 E. Cho, S. Han, D. Kim, H. Horii and S.-S. Nam, *J. Appl. Phys.*, 2011, **109**, 043705.

77 S. O. Kart, M. Tomak, M. Uludogan and T. Cagin, *Turk. J. Phys.*, 2006, **30**, 319.

78 S. L. Roux and V. Petkov, *J. Appl. Crystallogr.*, 2010, **43**, 181.

79 L. Pauling, *Proc. Natl. Acad. Sci. U. S. A.*, 1987, **84**, 4754.

80 L. Pauling, *Proc. Natl. Acad. Sci. U. S. A.*, 1950, **36**, 533.

81 L. Pauling, *The Nature of the Chemical Bond*, Cornell University Press, Ithaca, NY, 1975.

82 B. Hvolbæk, T. V. W. Janssens, B. S. Clausen, H. Falsig, C. H. Christensen and J. K. Nøorskov, *Nano Today*, 2007, **2**, 14.

83 T. Jiang, D. J. Mowbray, S. Dobrin, H. Falsig, B. Hvolbæk, T. Bligaard and J. K. Nørskov, *J. Phys. Chem. C*, 2009, **113**, 10548.

84 V. Petkov, Y. Ren, S. Shan, J. Luo and Ch. J. Zhong, *Nanoscale*, 2014, **6**, 532.

85 G. Brancolini, D. B. Kokh, L. Calzolai, R. C. Wade and S. Corni, *ACS Nano*, 2012, **6**, 9863.

86 V. Petkov, Y. Ren, I. Saratovsky, P. Pasten, S. J. Gurr, M. A. Hayward, K. Poppelmeier and J.-F. Galliard, *ACS Nano*, 2009, **3**, 441.

87 D. E. Mustafa, T. Yang, Z. Xuan, S. Chen, H. Tu and A. Zhang, *Plasmonics*, 2010, **5**, 221.

88 M. Abeykoon, C. D. Malliakas, P. Juhas, E. S. Bozin, M. G. Kanatzidis and S. J. L. Billinge, *Z. Kristallogr.*, 2012, **227**, 248.

89 G. Artioli, A. Pavese, M. Belloto, S. P. Collins and G. Lucchetti, *Amer. Mineral.*, 1996, **81**, 603.

90 V. Petkov, V. Parvanov, D. Tomalia, D. Swanson, D. Bergstrom and T. Vogt, *Solid State Commun.*, 2005, **134**, 671.

91 H. Zhang, B. Gilbert, F. Huang and J. F. Banfield, *Nature*, 2003, **424**, 1025.

92 I. D. Brown, *Chem. Rev.*, 2009, **109**, 6858.

93 T. D. Bennet, A. L. Goodwin, M. T. Dove, D. A. Keen, M. G. Tucker, E. R. Barney, A. K. Soper, E. G. Bithel, J.-C. Tan and A. K. Cheetham, *Phys. Rev. Lett.*, 2010, **104**, 115503.

94 V. Petkov, T. Ohta, Y. Hou and Y. Ren, *J. Phys. Chem. C*, 2007, **111**, 714.

95 V. Petkov, P. D. Cozzoli, R. Buonsanti, R. Cingolani and Y. Ren, *J. Am. Chem. Sci.*, 2009, **131**, 14264.

96 V. Petkov, C. M. Hessel, J. Ovtchinnikoff, A. Guillaussier, B. A. Korgel, X. Liu and C. Giordano, *Chem. Mater.*, 2013, **25**, 2365.

97 H. M. Rietveld, *J. Appl. Crystallogr.*, 1969, **2**, 65.

98 H. M. Rietveld, *Acta Crystallogr.*, 1966, **20**, 508.

99 A. Altomare, G. Cascarano, C. Giacovazzo, A. Guagliardi, M. C. Burla, G. Polidori and M. Camalli, *J. Appl. Crystallogr.*, 1994, **27**, 435.

100 W. I. F. David, K. Shankland, J. van de Streek, E. Pidcock, W. D. S. Motherwell and J. C. Cole, *J. Appl. Crystallogr.*, 2006, **39**, 920.